

# Reversible network reconnection model for simulating large deformation in dynamic tissue morphogenesis

Satoru Okuda · Yasuhiro Inoue · Mototsugu Eiraku ·  
Yoshiki Sasai · Taiji Adachi

Received: 24 February 2012 / Accepted: 7 August 2012 / Published online: 2 September 2012  
© Springer-Verlag 2012

**Abstract** Morphogenesis of tissues in organ development is accompanied by large three-dimensional (3D) deformations, in which mechanical interactions among multiple cells are spatiotemporally regulated. To reveal the deformation mechanisms, in this study, we developed the reversible network reconnection (RNR) model. The model is developed on the basis of 3D vertex model, which expresses a multicellular aggregate as a network composed of vertices. 3D vertex models have successfully simulated morphogenetic dynamics by expressing cellular rearrangements as network reconnections. However, the network reconnections in 3D vertex models can cause geometrical irreversibility, energetic inconsistency, and topological irreversibility, therefore inducing unphysical results and failures in simulating large deformations. To resolve these problems, we introduced (1) a new definition of the shapes of polygonal faces between cellular polyhedrons, (2) an improved condition for network reconnections, (3) a new condition for potential energy functions, and (4) a new constraint condition for the shapes of polygonal

faces that represent cell–cell boundaries. Mathematical and computational analyses demonstrated that geometrical irreversibility, energetic inconsistency, and topological irreversibility were resolved by suppressing the geometrical gaps in the network and avoiding the generation of irreversible network patterns in reconnections. Lastly, to demonstrate the applicability of the RNR model, we simulated tissue deformation of growing cell sheets and showed that our model can simulate large tissue deformations, in which large changes occur in the local curvatures and layer formations of tissues. Thus, the RNR model enables *in silico* recapitulation of complex tissue morphogenesis.

**Keywords** Tissue morphogenesis · Large deformation · Multicellular dynamics · Vertex model · Reversible network reconnection model

**Electronic supplementary material** The online version of this article (doi:[10.1007/s10237-012-0430-7](https://doi.org/10.1007/s10237-012-0430-7)) contains supplementary material, which is available to authorized users.

S. Okuda · Y. Inoue · T. Adachi (✉)  
Department of Biomechanics, Institute for Frontier  
Medical Sciences, Kyoto University, Kyoto, Japan  
e-mail: [adachi@frontier.kyoto-u.ac.jp](mailto:adachi@frontier.kyoto-u.ac.jp)

Y. Inoue  
e-mail: [inoue@frontier.kyoto-u.ac.jp](mailto:inoue@frontier.kyoto-u.ac.jp)

*Present Address:*  
T. Adachi  
53 Kawahara-cho, Shogoin, Sakyo-ku, Kyoto 606-8507, Japan

M. Eiraku · Y. Sasai  
Organogenesis and Neurogenesis Group, Center for Developmental  
Biology, RIKEN, Kobe, Japan

## 1 Introduction

Morphogenesis of multicellular organisms in organ development is accompanied by drastic tissue deformations in three-dimensional (3D) space, such as extensions (Heisenberg et al. 2000; Davies 2005), torsions (Taniguchi et al. 2011), foldings (Odell et al. 1981), invaginations (Odell et al. 1981; Letizia et al. 2011), and envaginations (Eiraku et al. 2011). In such deforming tissues, cellular configurations are rearranged with deforming cell–cell boundaries where neighboring cells adhere to one another (Weliky and Oster 1990; Lecuit and Lenne 2007). These dynamics at the multicellular scale are caused by cellular activities and interactions among neighboring cells such as apical constrictions (Lecuit et al. 2010), intercellular adhesions (Friedlander et al. 1989; Lecuit et al. 2008), and cell divisions (Farhadifar et al. 2007; Bellaiche and Segalen 2009). These cellular activities and interactions

generate internal and external mechanical forces at the sub-cellular scale, which are transferred through cell–cell boundaries to local cell populations. Effects of these forces on local cell populations accumulate during morphogenesis to form organs. Hence, the effects of biomechanical forces are important as well as biochemical factors, such as morphogen distributions and spatiotemporally regulated expression of genes (VanEssen 1997; Forgacs and Newman 2005; Ingber and Mammoto 2010). However, little is known about how cellular forces are orchestrated in deformations of local cell populations. To reveal these deformation mechanisms, it is necessary to analyze 3D tissue morphogenesis based on mechanical interactions among multiple cells.

Multicellular dynamics in aggregates are similar to those of multi-objects in soap froths and metal grains. Soap froths and metal grains have boundaries among their multi-objects as well as cells packed in aggregates. These boundaries are continuously connected to each other, and they compose a single net-like structure that can be regarded as a network composed of vertices and edges. Based on this characteristic structure, the dynamics of soap froths, metal grains, and cells have been theoretically and numerically analyzed using two-dimensional (2D) (Taniguchi et al. 2011; Odell et al. 1981; Weliky and Oster 1990; Farhadifar et al. 2007; Bragg and Nye 1947; Kikuchi 1956; Honda et al. 1982; Weaire and Kermode 1983, 1984; Nagai et al. 1988, 1990; Nagai and Honda 2001, 2009; Rauzi et al. 2008; Staple et al. 2010; Eiraku et al. 2012) and 3D (Nagai et al. 1990; Fuchizaki et al. 1995; Honda et al. 2004, 2008a,b) vertex models. Because configurations of multi-objects in aggregates can be rearranged, a rule of changing topological patterns in a network (hereafter referred to as “network reconnections”) is necessary to express the rearrangements of multi-objects in 2D (Honda et al. 1982) and 3D (Nagai et al. 1990) vertex models.

In general, network reconnections should satisfy the following conditions. First, the network patterns before and after reconnections should be topologically reversible. For computational simulations, if patterns cannot be topologically reversed to the original pattern, the computational algorithm may fail, or a part of the network may be locked. The latter causes unphysical frictions in the network, which reduce the viscosity in local regions of tissue. Second, the network patterns before and after reconnections should be geometrically reversible. If reconnections are geometrically irreversible, the difference between geometrical gaps could induce some unintentional drifts in vertex dynamics. For computational simulations, because drifts generated artificially by network reconnections cannot be distinguished from those generated by other physical factors such as potential energy gradients, the factors leading to morphogenetic dynamics become unclear. Third, energetic gaps should be self-consistent between their bidirectional reconnection

processes. If reconnections are energetically inconsistent, the difference between these energetic gaps also could induce some unintentional drifts in vertex dynamics. Thus, when employing vertex models with network reconnections for physical analysis, the above three important conditions must be satisfied.

Vertex models have already been applied to simulate tissue dynamics during morphogenesis. For example, the dynamics of cellular rearrangements and tissue deformations have been analyzed in terms of the mechanical behaviors of cells (Taniguchi et al. 2011; Odell et al. 1981; Weliky and Oster 1990; Farhadifar et al. 2007; Nagai and Honda 2001, 2009; Rauzi et al. 2008; Staple et al. 2010; Eiraku et al. 2012; Honda et al. 2004, 2008a,b). In particular, Honda’s 3D vertex model (2004) successfully determined how cells of early embryos are polarized (2008a) and how cellular intercalations drive tissue extensions in 3D space (2008b). To express cellular rearrangements, Honda’s model borrows a rule of network reconnections from 3D vertex models of soap froths (Nagai et al. 1990; Fuchizaki et al. 1995; Honda et al. 2004). To our knowledge, there is no alternative method to express cellular rearrangements in 3D vertex models. However, topological reversibility, geometrical reversibility, and energetic consistency described above have not yet been considered in a 3D vertex model. If these conditions are violated, 3D vertex models can possibly suffer from several problems. For example, because of topological irreversibility, a 3D vertex model cannot be directly applied to simulate large deformations under compression. In addition, because of geometrical irreversibility and energetic inconsistency, a 3D vertex model will numerically induce unintentional drifts in vertex dynamics. Therefore, to simulate large deformations during dynamic tissue morphogenesis under compression, a 3D vertex model should satisfy these important conditions.

In this study, to simulate large deformations of cell aggregates during tissue morphogenesis in 3D space on the basis of mechanical forces at the subcellular scale, we propose an improved 3D vertex model. To satisfy both geometrical reversibility and energetic consistency, the following three conditions are introduced: (1) a new definition of shapes of polygonal faces, (2) an improved condition for network reconnections, and (3) a new condition for potential energy functions. To satisfy topological reversibility, a fourth condition is introduced: (4) a new constraint condition for networks. To distinguish our proposed model from other vertex models, we refer to our model as the reversible network reconnection (RNR) model. In Sect. 2, we propose the RNR model that involves conditions 1–4 are proposed. In Sect. 3, we theoretically and computationally analyze how geometrical irreversibility, energetic inconsistency, and topological irreversibility are resolved in the RNR model. In Sect. 3.5, to demonstrate the applicability of the RNR model, we simulate the morphogenetic dynamics of a growing cell sheet under

compression. In Sect. 4, we discuss the applicability and limitations of the RNR model, and we state future perspectives. In Sect. 5, we summarize the paper and provide concluding remarks.

## 2 Reversible network reconnection model

### 2.1 Shape and dynamics of a multicellular aggregate

The RNR model expresses the shape of a single cell as a single polyhedron (Fig. 1). Polyhedrons are composed of vertices and edges that are shared by neighboring polyhedrons. Vertices and edges compose a network that represents the whole shape of the aggregate. In the network, each vertex is connected to exactly four edges. In addition, polygonal faces compartmentalize neighboring polyhedrons.

To express the dynamics of a multicellular aggregate during morphogenesis, an equation that describes the motion of the  $i$ th vertex is introduced as

$$\eta \frac{d\mathbf{r}_i}{dt} = -\frac{\partial U}{\partial \mathbf{r}_i}. \quad (1)$$

The left-hand side of Eq. (1) indicates a frictional force exerted on the  $i$ th vertex, where  $\eta$  indicates a friction coefficient, and  $\mathbf{r}_i$  indicates the position vector of the  $i$ th vertex. The right-hand side of Eq. (1) indicates a conservative force, where  $U$  indicates a potential energy expressing cellular mechanical behaviors that can be generally expressed by

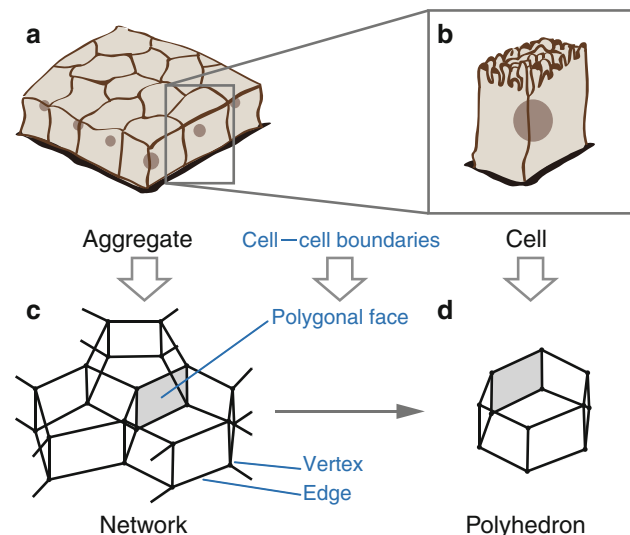


**Fig. 1** Model shapes of a multicellular aggregate. **a** An aggregate composed of cells. **b** A single cell. **c** A network that represents a cell aggregate. The network is composed of vertices and edges (solid lines). The position vector of the  $i$ th vertex is denoted by  $\mathbf{r}_i$ . Polygonal faces (like the gray area) compartmentalize the network. **d** A polyhedron that represents a single cell

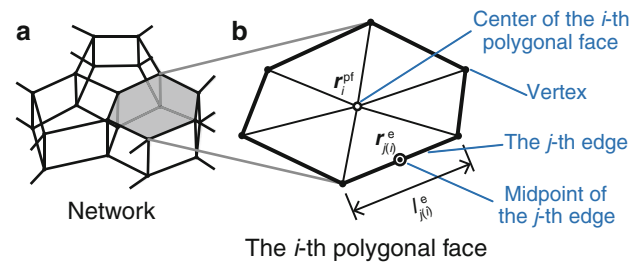


**Fig. 2** Definition of polygonal face shapes in the RNR model. **a** A network representing a cell aggregate. **b** The  $i$ th polygonal face corresponding to the gray area in (a). Solid thick lines indicate edges composing a polygonal face, and solid thin lines indicate edges composing triangles in the polygonal face. A single circle indicates the center of the  $i$ th polygonal face, whose position is denoted by  $\mathbf{r}_i^{\text{pf}}$ . Two concentric circles indicate the midpoint of the  $j$ th edge composing the  $i$ th polygonal face, whose position is denoted by  $\mathbf{r}_{j(i)}^e$ . The length of the  $j$ th edge composing the  $i$ th polygonal face is denoted by  $l_{j(i)}^e$

$$U = U^{\text{cell}} + U^{\text{cell-cell}} + U^{\text{cell-ext}}. \quad (2)$$

Here potential energy  $U^{\text{cell}}$  indicates mechanical behaviors of individual cells such as volume elasticity, surface elasticity, apical constriction, and other effects of intracellular structures and activities. Potential energy  $U^{\text{cell-cell}}$  indicates interactions between cells such as cell–cell adhesions at intercellular junctions. Potential energy  $U^{\text{cell-ext}}$  indicates interactions between cells and extracellular structures such as extracellular matrixes, basement membranes, and solvent liquids. In addition,  $U^{\text{cell}}$ ,  $U^{\text{cell-cell}}$ , and  $U^{\text{cell-ext}}$  express changes in cellular mechanical behaviors induced by morphogens generated inside the cell, morphogens transported from surrounding cells, and morphogens transported from extracellular structures, respectively.

In the case that a face involving more than three vertices deviates from a flat plane, shapes of the faces cannot be determined only from their vertex positions. It is necessary to show how to divide a non-flat face into several triangles. To establish cellular shapes, we define shapes of the polygonal faces as follows:

**Condition 1** The shape of a polygonal face that has four or more edges is defined as radially arranged triangles composed of each edge and the center point of the polygonal face (Fig. 2). The position vector of the center point of the  $i$ th polygonal face,  $\mathbf{r}_i^{\text{pf}}$ , is defined as

$$\mathbf{r}_i^{\text{pf}} = \frac{\sum_{j(i)}^{\text{side}} l_{j(i)}^e \mathbf{r}_{j(i)}^e}{\sum_{j(i)}^{\text{side}} l_{j(i)}^e}, \quad (3)$$

where  $\sum_{j(i)}^{\text{side}}$  indicates the summation of side edges of the  $i$ th polygonal face. The length  $l_{j(i)}^e$  and position vector  $\mathbf{r}_{j(i)}^e$  indicate the length and midpoint of the  $j$ th edge in the  $i$ th polygonal face, respectively.

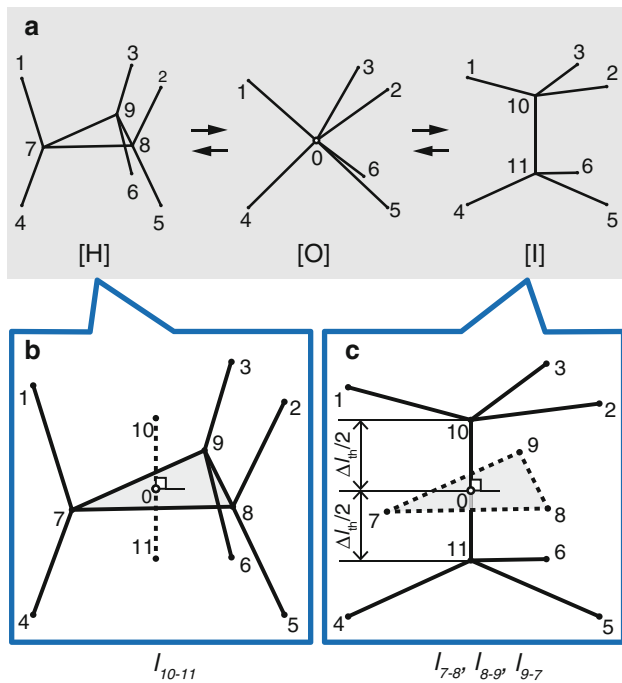


**Fig. 3** Network reconnection rule employed in the RNR model. The numbers indicate serial vertices, and solid lines indicate edges between vertices. **a** Reconnected patterns (Nagai et al. 1990; Fuchizaki et al. 1995; Honda et al. 2004). The trigonal face composed of the vertices labeled 7, 8, and 9 in [H] is replaced by the edge composed of the vertices labeled 10 and 11 in [I] in bidirections when their geometries satisfy condition 2 in the RNR model. The point labeled 0 in [O] indicates the center of the reconnection. **b** Pattern [H] reconnected from [I], in which a length of the edge composed of the vertices labeled 10 and 11,  $l_{10-11}$ , satisfies condition 2. **c** Pattern [I] reconnected from [H], in which lengths of the edges composed of the vertices labeled 7, 8, and 9, denoted by  $l_{7-8}$ ,  $l_{8-9}$ , and  $l_{9-7}$ , respectively, satisfy condition 2

## 2.2 Cellular rearrangements in an aggregate

To express cellular rearrangements, we introduce a rule of network reconnections (Nagai et al. 1990; Fuchizaki et al. 1995; Honda et al. 2004). According to the reconnection rule, the network is reconnected between [H] and [I] as shown in Fig. 3, and reconnection events are generated when the network satisfies the geometrical condition. However, reconnections using the geometrical condition used in Honda's model occasionally induce unintentional drifts because of geometrical gaps and the energetic inconsistency between bidirectional reconnection processes (shown in Sect. 3.1).

To resolve the geometrical irreversibility and energetic inconsistency, we improve the geometrical condition as follows:

**Condition 2** If the maximum length of edges relating to reconnections ( $l_{7-8}$ ,  $l_{8-9}$ ,  $l_{9-7}$ , and  $l_{10-11}$ ) becomes shorter than the threshold value  $\Delta l_{th}$ , a network is reconnected.

In addition, we introduce a condition for the potential energy function as follows:

**Condition 3** The function of potential energy  $U$  in Eq. (2) should satisfy the following relationship:

$$\Delta U_{I \rightarrow H} + \Delta U_{H \rightarrow I} = O(\Delta l_{th}), \quad (4)$$

where  $\Delta U_{I \rightarrow H}$  and  $\Delta U_{H \rightarrow I}$  indicate energetic gaps in two processes of reconnection between patterns [H] and [I].

Note that the definitions of position vectors of vertices after reconnection are slightly different from those employed in Honda's model (see Appendix 1).

In addition to the above geometrical irreversibility and energetic inconsistency, 3D vertex models can possibly suffer from topological irreversibility, in that the reconnection rule generates network patterns to which this rule cannot be applied (shown in Sect. 3.3). To resolve this topological irreversibility, we introduce the following constraint condition:

**Condition 4** The network topology satisfies the following conditions:

- (i) Two edges never share two vertices simultaneously.
- (ii) Two polygonal faces never share two or more edges simultaneously.

This condition constrains the network's topology but not its geometry; therefore, shapes of polygonal faces can deform out of plane. This is consistent with the observed undulating shapes of cell-cell boundaries. Note that condition 4 is not the same as that employed in Honda's model. This is because the network patterns generated under condition 2 are not similar to those under the condition employed in Honda's model.

## 3 Physical and mathematical insights into improvements of the model

### 3.1 Geometrical gaps in network reconnections

Because the reconnection rule is related to five lengths from point 0 to the vertices 7, 8, 9, 10, and 11 in Fig. 3a, the geometrical reversibility of network reconnection can be formulated as

$$\Delta r_{H \leftrightarrow I}^{vt} = 0, \quad (5)$$

$$\Delta r_{H \leftrightarrow I}^{pf} = 0, \quad (6)$$

where  $\Delta r_{H \leftrightarrow I}^{vt}$  indicates the maximum of the five lengths from point 0, and  $\Delta r_{H \leftrightarrow I}^{pf}$  indicates the displacements of center points of polygonal faces in bidirectional reconnection between [H] and [I]. If both Eqs. (5) and (6) are satisfied, the network geometries before and after reconnection are exactly equal. To clarify whether the RNR model satisfies geometrical reversibility, we theoretically estimate



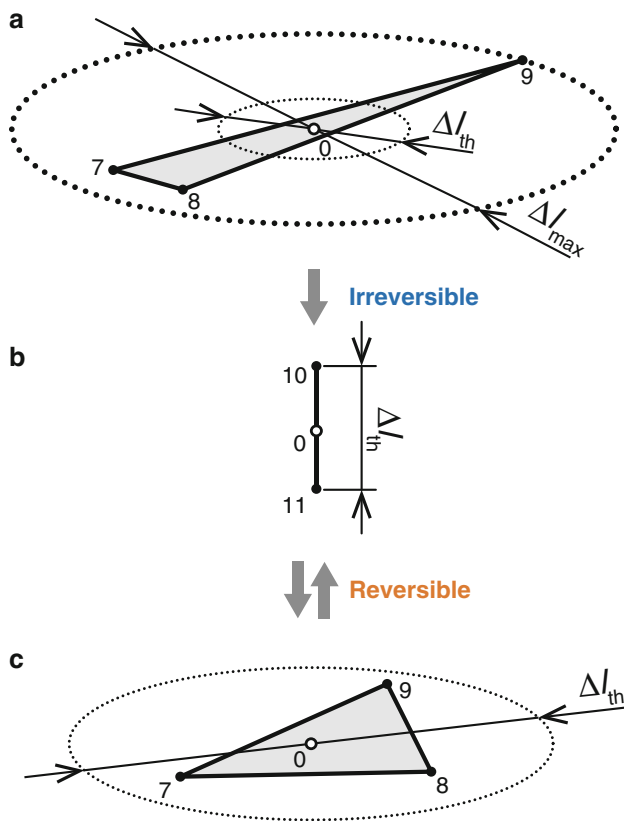


**Fig. 4** Geometrical gaps of vertex positions induced by reconnections from [H] to [O] in Fig. 3. **a** A positional relationship of vertices in [H] generating large gaps under condition H. The *thin dotted line* indicates a circle of radius  $\Delta l_{th}$  and centered at point 0. The *thick dotted line* indicates a circle of radius of  $\Delta l_{max}$  and centered at point 0. Here  $\Delta l_{max}$  can be much longer than  $\Delta l_{th}$ . **b** A positional relationship of vertices in [I] under both conditions H and 2. **c** A positional relationship of vertices in [H] under condition 2 employed in the RNR model. The lengths from 0 to 7, 8, and 9 must be smaller than  $\Delta l_{th}$  under our proposed condition

the geometrical gaps in bidirectional reconnection processes between patterns [H] and [I] in each case employing condition 1 or 2.

### 3.1.1 Geometrical gaps of vertices

**Geometrical gaps of vertices under condition 2** To reduce geometrical gaps generated by reconnections, condition 2 is introduced in the RNR model. To confirm the effectiveness of condition 2, these displacements are estimated with and without conditions 2 by measuring the maximum value of the five lengths from point 0 to the vertices 7, 8, 9, 10, and 11.

In the RNR model, because condition 2 is introduced, the maximum length  $\Delta r_{H \leftrightarrow I}^{vt}$  satisfies the following relationship:

$$\Delta r_{H \leftrightarrow I}^{vt} \leq \Delta l_{th}, \quad (7)$$

as shown in Fig. 4c (derived in Appendix.2). Here Eq. (7) leads to Eq. (5) in the zero limit of  $\Delta l_{th}$ . Thus, under condition 2, we can suppress the gaps of vertex positions in reconnections by choosing an appropriate value of  $\Delta l_{th}$ .

**Geometrical gaps of vertices under the condition employed in Honda's model** To evaluate the effectiveness of condition 2, geometrical gaps in the RNR model is compared with those of Honda's model. Honda's model (2004) employs the following network reconnection condition: If the minimum length of edges relating to the reconnections ( $l_{7-8}$ ,  $l_{8-9}$ ,  $l_{9-7}$ , and  $l_{10-11}$ ) becomes shorter than the threshold value  $\Delta l_{th}$ , a network is reconnected (hereafter referred to as condition H). Under condition H, the maximum of the five lengths from point 0,  $\Delta r_{H \leftrightarrow I}^{vt}$ , satisfies the following relationship:

$$\Delta r_{H \leftrightarrow I}^{vt} \leq \Delta l_{max}, \quad (8)$$

as shown in Fig. 4a (derived from Appendix.2). Here  $\Delta l_{max}$  indicates the maximum distance from point 0 to vertices 7, 8, and 9. Because length  $\Delta l_{max}$  is independent of  $\Delta l_{th}$ , the gaps can become much larger than  $\Delta l_{th}$ .

Employing condition H, the geometrical gaps in reconnections from [H] to [I] can be much larger than  $\Delta l_{th}$ , whereas those in reconnections from [I] to [H] must be on the order of  $\Delta l_{th}$  (as shown in Fig. 4a, b). Thus, occasionally the network geometry after reconnections from [I] to [H] cannot be reversed. On the other hand, employing condition 2, the network geometry is always reversible because the gaps in reconnections from [H] to [I] are on the order of  $\Delta l_{th}$ , as in Eq. (7) (see Fig. 4b, c).

### 3.1.2 Geometrical gaps of polygonal centers

**Geometrical gaps of polygonal centers under condition 1** The center points of polygonal faces can be displaced by vertex displacements, additions, and eliminations during reconnections (Fig. 5). To reduce these displacements of polygonal centers, condition 1 is introduced in the RNR model. To confirm the effectiveness of condition 1, the center displacements are measured as follows.

Center displacements due to vertex displacements shown in Fig. 5a are estimated as follows. When the  $s$ th vertex in the  $i$ th polygonal face is displaced by  $\Delta \mathbf{r}_{s(i)}$ , the center displacement of the  $i$ th polygonal face  $\Delta^d \mathbf{r}_i^{pf}$  when employing condition 1 satisfies the following relationship derived in Appendix.3.1.

$$\left| \Delta^d \mathbf{r}_{s(i)}^{pf} \right|_{H \leftrightarrow I} = O(|\Delta \mathbf{r}_{s(i)}|) \quad (9)$$

Center displacements due to vertex additions shown in Fig. 5b are estimated as follows. A single new vertex is generated between the  $t$ th and  $(t+1)$ th vertices in the  $i$ th

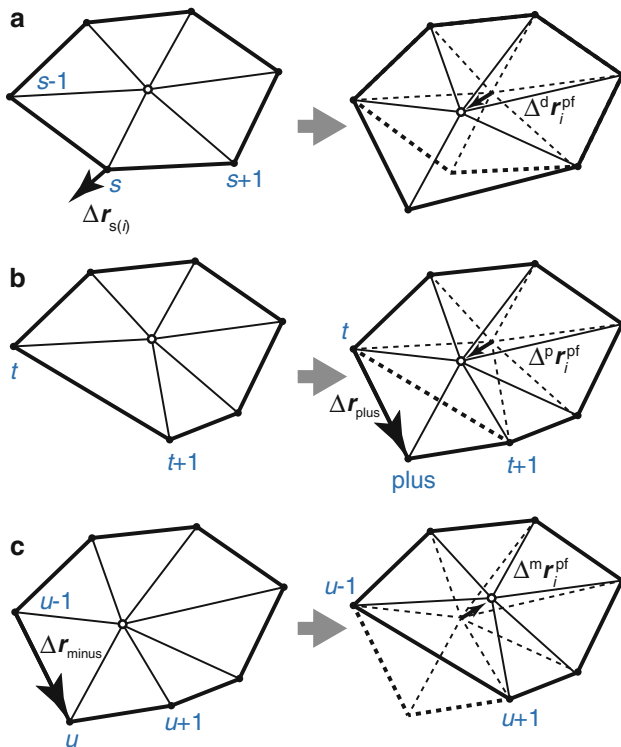


**Fig. 5** Displacement of the center point of a polygonal face. *Solid thick lines* indicate edges of polygonal faces. *Solid thin lines* indicate edges composing triangles in a polygonal face. An *open circle* indicates the center of a face. *Thin arrows* indicate displacement vectors. The *left and right side* illustrations indicate the shapes of polygonal faces before and after changes, respectively. **a** The center point of a polygonal face is displaced by vertex displacements. The displacement of the  $s$ th vertex in the  $i$ th polygonal face is denoted by  $\Delta r_{s(i)}$ , and the center displacement of the  $i$ th polygonal face is denoted by  $\Delta^d r_i^{pf}$ . **b** The center point of a polygonal face is displaced by generating a new (plus) vertex. The distance from the generated vertex to the  $t$ th vertex in the  $i$ th polygonal face is denoted by  $|\Delta r_{plus}|$ , and the center displacement of the  $i$ th polygonal face is denoted by  $\Delta^p r_i^{pf}$ . **c** The center point of a polygonal face is displaced by eliminating a vertex. The distance from the  $u$ th vertex to the  $(u-1)$ th vertex is denoted by  $|\Delta r_{minus}|$ , and the center displacement of the  $i$ th polygonal face is denoted by  $\Delta^m r_i^{pf}$

polygonal face. Assuming that the distance from the generated vertex to the  $t$ th vertex  $|\Delta r_{plus}|$  is much smaller than the length scale of the polygonal face, that is,

$$|\Delta r_{plus}| \ll |r_{t+1(i)} - r_{t(i)}|, \quad (10)$$

the center displacement of the  $i$ th polygonal face  $\Delta^p r_i^{pf}$  in case employing condition 1 satisfies the following relationship derived in Appendix.3.2.

$$|\Delta^p r_i^{pf}|_{H \leftrightarrow I} = O(|\Delta r_{plus}|) \quad (11)$$

Center displacements due to vertex eliminations shown in Fig. 5c are estimated as follows. The  $u$ th vertex is eliminated in the  $i$ th polygonal face. Assuming that the distance from

the  $u$ th vertex to the  $(u+1)$ th vertex  $|\Delta r_{minus}|$  is smaller than the length scale of the polygonal face, i.e.,

$$|\Delta r_{minus}| \ll |r_{u+1(i)} - r_{u-1(i)}|, \quad (12)$$

the center displacement of the  $i$ th polygonal face  $\Delta^m r_i^{pf}$  in case employing condition 1 satisfies the following relationship derived in Appendix.3.3.

$$|\Delta^m r_i^{pf}|_{H \leftrightarrow I} = O(|\Delta r_{minus}|) \quad (13)$$

From these results, under conditions 1 and 2, the maximum length of  $|\Delta^d r_i^{pf}|$ ,  $|\Delta^p r_i^{pf}|$ , and  $|\Delta^m r_i^{pf}|$ , denoted by  $\Delta r_{H \leftrightarrow I}^{pf}$ , satisfies the following relationship:

$$\Delta r_{H \leftrightarrow I}^{pf} = O(\Delta r_{H \leftrightarrow I}^{vt}). \quad (14)$$

Substituting Eqs. (7) into (14),  $\Delta r_{H \leftrightarrow I}^{pf}$  is rewritten as

$$\Delta r_{H \leftrightarrow I}^{pf} = O(\Delta l_{th}), \quad (15)$$

which satisfies Eq. (6) in the zero limit of  $\Delta l_{th}$ . Thus, under conditions 1 and 2, we can suppress the center displacements in reconnections by choosing an appropriate small value of  $\Delta l_{th}$ .

*Geometrical gaps of polygonal centers with the simple definition of a polygonal face* To evaluate the effectiveness of condition 1, the center displacements in the RNR model are compared with those when employing a simple definition of a polygonal center:

$$r_i^{pf} = \frac{1}{n_i^{v}} \sum_{j(i)}^{vertex} r_{j(i)}, \quad (16)$$

where  $\sum_{j(i)}^{vertex}$  indicates a summation over all cells. The variable  $n_i^{v}$  indicates the number of vertices in the  $i$ th polygonal face. When employing the simple definition, the center displacements due to vertex displacements, additions, and eliminations are estimated as

$$(\Delta^d r_i^{pf})_{H \leftrightarrow I} = \frac{1}{n_i^{v}} \Delta r_{s(i)}, \quad (17)$$

$$(\Delta^p r_i^{pf})_{H \leftrightarrow I} = \frac{1}{n_i^{v} + 1} (r_{plus} - r_i^{pf}), \quad (18)$$

$$(\Delta^m r_i^{pf})_{H \leftrightarrow I} = -\frac{1}{n_i^{v} - 1} (r_{u(i)} - r_i^{pf}), \quad (19)$$

respectively. Here,  $r_{plus}$  and  $r_{u(i)}$  indicate position vectors of added and eliminated vertices in Fig. 5b, c, respectively. The values of the center displacements shown in Eqs. (17, 18), and (19) can be much larger than the order of  $\Delta l_{th}$ , even when employing condition 2 and Eqs. (10) and (12).

### 3.1.3 Area gaps of polygonal faces

If geometrical reversibility is satisfied, the gap in cellular geometrical properties during reconnections is zero. For example, when the  $i$ th polygonal center is displaced from  $\mathbf{r}_i^{\text{pf}}$  to  $\mathbf{r}_i^{\text{pf}} + \Delta \mathbf{r}_i^{\text{pf}}$  by reconnections, the area gap of the  $j$ th trigonal component of the  $i$ th polygonal face, denoted by  $\Delta s_{j(i)}^{\text{pf,tc}}$ , should be zero, that is,

$$|\Delta s_{j(i)}^{\text{pf,tc}}| = 0. \quad (20)$$

To clarify whether such gaps in cellular geometrical properties are suppressed in the RNR model, we estimate the area gaps generated by the displacements of polygonal centers as an example.

Area gaps generated by the displacements of polygonal centers are estimated as follows:

$$|\Delta s_{j(i)}^{\text{pf,tc}}| = |\mathbf{h}_{j(i)}^{\text{tc}} \times \Delta \mathbf{r}_i^{\text{pf}}|, \quad (21)$$

where

$$\mathbf{h}_{j(i)}^{\text{tc}} = \frac{\mathbf{r}_{j(i)} + \mathbf{r}_{j+1(i)}}{2} - \mathbf{r}_i^{\text{pf}}. \quad (22)$$

Because  $\mathbf{h}_{j(i)}^{\text{tc}}$  is a vector in a plane of the  $j$ th trigonal component, the extent of the area gap tends to depend on the deviations of polygonal faces from a flat plane.

*Area gaps of polygonal faces under condition 1* Assuming conditions 1 and 2, we substitute Eqs. (15) into (21) and get the following equation:

$$|\Delta s_{j(i)}^{\text{pf,tc}}|_{\text{H} \leftrightarrow \text{I}} = O(\Delta l_{\text{th}}), \quad (23)$$

which satisfies Eq. (20) in the zero limit of  $\Delta l_{\text{th}}$ . Thus, under conditions 1 and 2, we can suppress the area gaps of polygonal faces during reconnections by choosing an appropriate small value of  $\Delta l_{\text{th}}$ .

*Area gaps of a polygonal faces in the simple definition of a polygonal face* As an example, assuming the simple definition of a polygonal center, we substitute Eqs. (17, 18), and (19) into (21) and get

$$|\Delta s_{j(i)}^{\text{pf,tc}}|_{\text{H} \leftrightarrow \text{I}}^{\text{d}} = \frac{1}{n_i^{\text{v}}} |\mathbf{h}_{j(i)}^{\text{tc}} \times \Delta \mathbf{r}_{s(i)}|, \quad (24)$$

$$|\Delta s_{j(i)}^{\text{pf,tc}}|_{\text{H} \leftrightarrow \text{I}}^{\text{p}} = \frac{1}{n_i^{\text{v}} + 1} |\mathbf{h}_{j(i)}^{\text{tc}} \times (\mathbf{r}_{\text{plus}} - \mathbf{r}_i^{\text{pf}})|, \quad (25)$$

$$|\Delta s_{j(i)}^{\text{pf,tc}}|_{\text{H} \leftrightarrow \text{I}}^{\text{m}} = \frac{1}{n_i^{\text{v}} - 1} |\mathbf{h}_{j(i)}^{\text{tc}} \times (\mathbf{r}_{u(i)} - \mathbf{r}_i^{\text{pf}})|, \quad (26)$$

respectively. These values can be much larger than the order of  $\Delta l_{\text{th}}$  when employing either condition 2 or H.

### 3.2 Energetic gaps in network reconnections

Energetic consistency for the reconnection rule can be formulated as

$$\Delta U_{\text{I} \rightarrow \text{H}} + \Delta U_{\text{H} \rightarrow \text{I}} = 0. \quad (27)$$

If a function of  $U$  satisfies condition 3, then energetic consistency is satisfied in the zero limit of  $\Delta l_{\text{th}}$ . However, it is not trivial that functions of the potential energy generally used for simulating tissue morphogenesis satisfy condition 3. Therefore, to confirm that such functions of the potential energy  $U$  satisfy condition 3, we estimate the energetic gaps in bidirectional reconnections in the Honda's and RNR models using functions of  $U$  introduced here. The potential energy  $U$  is commonly written as a function of lengths of edges ( $l$ ), areas of polygonal faces ( $s$ ), and volumes of cells ( $v$ ) (Taniguchi et al. 2011; Farhadifar et al. 2007; Nagai and Honda 2001, 2009; Rauzi et al. 2008; Staple et al. 2010; Eiraku et al. 2012; Honda et al. 2004, 2008a,b)

$$U = U(l, s, v). \quad (28)$$

Here the maximum and minimum exponents of  $l$ ,  $s$ , and  $v$  are denoted by  $m$  and  $n$ , respectively.

The gaps of  $l$ ,  $s$ , and  $v$  in reconnections are denoted by  $\Delta l$ ,  $\Delta s$ , and  $\Delta v$ , respectively. Using Eqs. (7) and (15), the gaps under conditions 1 and 2,  $\Delta l_{\text{H} \leftrightarrow \text{I}}^{\text{O}}$ ,  $\Delta s_{\text{H} \leftrightarrow \text{I}}^{\text{O}}$ , and  $\Delta v_{\text{H} \leftrightarrow \text{I}}^{\text{O}}$ , are estimated as

$$\Delta l_{\text{H} \leftrightarrow \text{I}}^{\text{O}} = O(\Delta l_{\text{th}}), \quad (29)$$

$$\Delta s_{\text{H} \leftrightarrow \text{I}}^{\text{O}} = O(\Delta l_{\text{th}}), \quad (30)$$

$$\Delta v_{\text{H} \leftrightarrow \text{I}}^{\text{O}} = O(\Delta l_{\text{th}}). \quad (31)$$

Then, using Eqs. (29–31), the gap of the potential energy  $U$  under condition 2,  $\Delta U_{\text{H} \leftrightarrow \text{I}}^{\text{O}}$ , is estimated as

$$\Delta U_{\text{H} \leftrightarrow \text{I}}^{\text{O}} = O((\Delta l_{\text{th}})^n), \quad (32)$$

which satisfies condition 3. Namely,  $U$  in Eq. (28) satisfies Eq. (27) in the zero limit of  $\Delta l_{\text{th}}$ . Thus, by choosing an appropriate value of  $\Delta l_{\text{th}}$ , the RNR model can satisfy energetic consistency in network reconnections.

In contrast, using Eq. (8), these gaps under condition H,  $\Delta l_{\text{H} \leftrightarrow \text{I}}^{\text{H}}$ ,  $\Delta s_{\text{H} \leftrightarrow \text{I}}^{\text{H}}$ , and  $\Delta v_{\text{H} \leftrightarrow \text{I}}^{\text{H}}$  are estimated as

$$\Delta l_{\text{H} \leftrightarrow \text{I}}^{\text{H}} = O(\Delta l_{\text{max}}), \quad (33)$$

$$\Delta s_{\text{H} \leftrightarrow \text{I}}^{\text{H}} = O(\Delta l_{\text{max}}), \quad (34)$$

$$\Delta v_{\text{H} \leftrightarrow \text{I}}^{\text{H}} = O(\Delta l_{\text{max}}). \quad (35)$$

Then, using Eqs. (33–35), the gap of the potential energy  $U$  under condition H,  $\Delta U_{\text{H} \leftrightarrow \text{I}}^{\text{H}}$ , is estimated as

$$\Delta U_{\text{H} \leftrightarrow \text{I}}^{\text{H}} = \begin{cases} O((\Delta l_{\text{max}})^m) & : \Delta l_{\text{max}} \geq 1, \\ O((\Delta l_{\text{max}})^n) & : \Delta l_{\text{max}} < 1, \end{cases} \quad (36)$$

which does not satisfy condition 3. Thus, here energetic consistency is not satisfied under condition H.

### 3.3 Two irreversible network patterns in reconnections

There are at least two network patterns  $[\alpha]$  and  $[\beta]$  shown in Fig. 6 to which the reconnection rule cannot be applied (see Appendix.4). Pattern  $[\alpha]$  is avoided by condition 4(i) because it has double edges sharing two vertices simultaneously. Pattern  $[\beta]$  has two trigonal faces neighboring each other. Pattern  $[\beta]$  is avoided by condition 4(ii) because it must have two faces that share two or more edges simultaneously. Thus,  $[\alpha]$  and  $[\beta]$  are avoided by condition 4. Condition 4(ii) avoids not only pattern  $[\beta]$  but also pattern  $[\gamma]$ , which has two faces sharing two or more edges simultaneously, as shown in Fig. 6.

### 3.4 Reconnection simulations of a network

Employing condition 4, patterns  $[\alpha]$  and  $[\beta]$  are avoided for candidates reconnected between [H] and [I] in Fig. 3. However, these two patterns may not represent all irreversible patterns. Hence, to clarify the topological reversibility of the reconnections with condition 4, we performed reconnection simulations. In these simulations, networks must randomly reconnect without condition 2, and the positional coordinates of the vertices are fixed by excluding vertex dynamics in Eq. (1). To confirm the effectiveness of condition 4, we

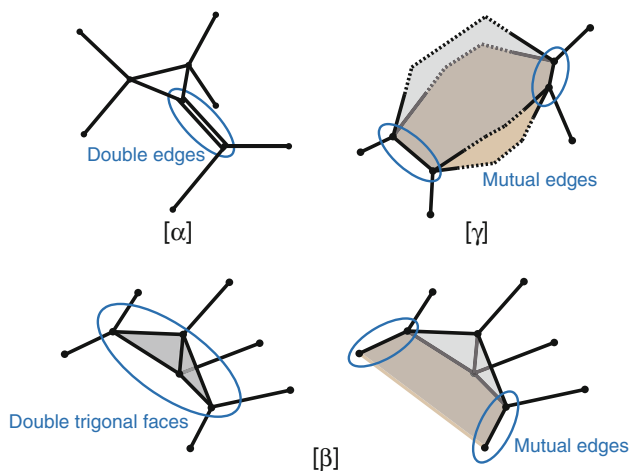


**Fig. 6** Network patterns related to reconnection inconsistencies and their remediation. Patterns  $[\alpha]$  and  $[\beta]$  indicate network patterns to which the reconnection rule in Fig. 3 cannot be applied. Pattern  $[\alpha]$ , which has double edges sharing the same two vertices, is avoided by condition 4(i). Pattern  $[\gamma]$ , which has two or more edges shared by two polygonal faces, is avoided by condition 4(ii). Bottom two illustrations indicate identical pattern  $[\beta]$ . Pattern  $[\beta]$ , which has two neighboring trigonal faces, is avoided by condition 4(ii). This is because pattern  $[\beta]$ , which also has two or more edges shared by two polygonal faces, is a necessary condition for pattern  $[\gamma]$

performed simulations using reconnections both with and without condition 4. Note that in terms of network topology, the model with condition 4 corresponds to the RNR model, while that without condition 4 does not correspond to Honda's model. In these simulations, reconnection trials are conducted for every edge and every trigonal face at every step. In addition, the bidirectional transition probability of reconnections between [H] and [I] is set to 0.01.

Figure 7a shows the initial conditions of the simulation. The system box size is set to  $6 \times 6 \times 6$ . In the system, 250 isotropic dodecahedrons, each having a volume set to 1, are homogeneously placed in a hexagonal close-packed structure. Periodic boundaries are employed for the  $x$ -,  $y$ -, and  $z$ -axes. To evaluate mean behaviors, five random samples are obtained.

Figure 7b shows that simulations without condition 4 could not run beyond two steps on average. This is because the above-mentioned irreversible patterns were generated. In contrast, simulations with condition 4 could run over the entire employed parameter space. Furthermore, bidirectional reconnections between [H] and [I] were conducted at every step, and the number of vertices and frequencies of reconnections increased with the number of steps, as shown in Fig. 7c.

### 3.5 Simulations of tissue growth

To demonstrate the applicability of the RNR model for simulating compressive large deformations, we simulated the morphogenetic dynamics of a monolayered growing cell sheet. The growing cell sheet involves growing cells whose volumes increase with time. In these simulations, we evaluate the effectiveness of condition 4 on the applicability of the RNR model (which includes condition 4), and we also evaluate a model without condition 4 (which is not Honda's model in terms of network topology). Because conditions 1, 2, and 3 must be employed to satisfy geometrical reversibility and energetic consistency (as described later) and because they are independent of topological irreversibility that causes failures in simulations of compressive large deformations, both models involve these three conditions.

To evaluate the effectiveness of condition 4, in this study, the mechanical behaviors of cells are simply expressed by the potential energy  $U$  as

$$U = U^v + U^{\text{int}}, \quad (37)$$

as employed in previous studies using Honda's model (2004, 2008a, 2008b). The potential energy  $U^v$  indicates the cellular volume elasticity, and the potential energy  $U^{\text{int}}$  indicates the interface energy at cellular boundaries. The potential energy  $U^v$  is expressed as



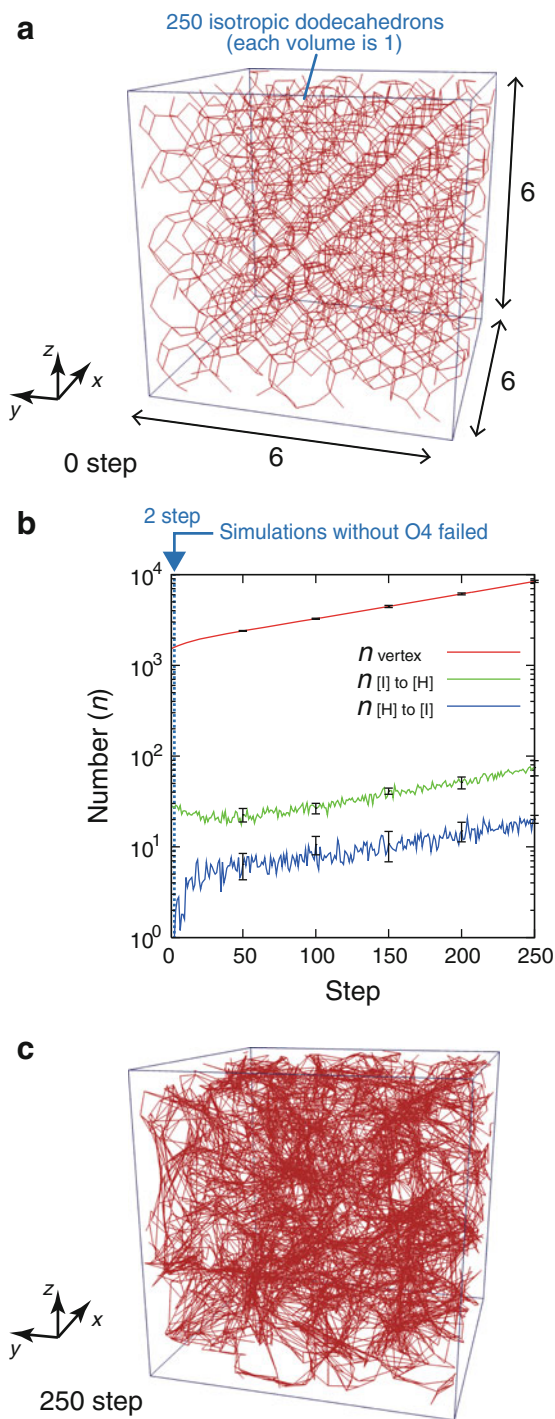


**Fig. 7** Reconnection simulations. **a** Initial condition of the network. The system box is  $6 \times 6 \times 6$ , in which 250 isotropic tetradodecahedrons are homogeneously placed in a hexagonal close-packed structure. A periodic boundary condition is employed for expressing the  $x$ - $y$ - $z$  boundaries. Red lines indicate edges of the network. **b** The number of vertices, number of reconnections from [I] to [H], and number of reconnections from [H] to [I] as a function of time  $t$ , resulting from simulations with condition 4 employed in the RNR model. Simulations without condition 4 failed at an average step of 2.0. Error bars indicate standard deviations of the data at individual steps. **c** Snapshot of the network at the 250th step

$$U^v = \sum_i^{\text{cell}} \frac{1}{2} k^{\text{cv}} \left( \frac{v_i}{v_{i \text{ eq}}} - 1 \right)^2, \quad (38)$$

where  $\sum_i^{\text{cell}}$  indicates a summation over all cells. The constant  $k^{\text{cv}}$  indicates the strength of the potential energy. Variables  $v_i$  and  $v_{i \text{ eq}}$  indicate the current and equilibrium volume of the  $i$ th cell, respectively. The potential energy  $U^{\text{int}}$  is expressed as

$$U^{\text{int}} = \sum_i^{\text{cell}} \sum_{j(>i)}^{\text{cell}} \epsilon^{\text{cc}} s_{ij}^{\text{cc}} + \sum_i^{\text{cell}} \epsilon^{\text{co}} s_i^{\text{co}}, \quad (39)$$

where the constants  $\epsilon^{\text{cc}}$  and  $\epsilon^{\text{co}}$  indicate the interface energy density between the  $i$ th and  $j$ th cells and that between the  $i$ th cell and extracellular substances, respectively. Variables  $s_{ij}^{\text{cc}}$  and  $s_i^{\text{co}}$  indicate the boundary area between the  $i$ th and  $j$ th cells and that between the  $i$ th cell and outside, respectively. Note that the  $U$  introduced here satisfies condition 3 in the RNR model. Numerical integrals of Eq. (1) are performed using the improved Euler's method with a time step of  $\Delta t$ . Reconnection trials are conducted for every edge and trigonal face at every time interval of  $\Delta t_r$ .

Figure 8a shows the initial condition of the simulation, in which 400 hexagonal-cylinder-shaped cells are homogeneously placed as in a monolayered cell sheet on the curved surface:

$$z = A^{\text{ic}} \cos \left( 2\pi \frac{x}{L_x} \right) \cos \left( 2\pi \frac{y}{L_y} \right), \quad (40)$$

where  $L_x$  and  $L_y$  indicate the lengths of the system box in the  $x$  and  $y$  directions, respectively. The constant  $A^{\text{ic}}$  indicates the amplitude of the initial undulation of the curved surface. Then, vertex positions are randomly displaced with a variance of 0.001. Periodic boundaries are employed for  $x$ - and  $y$ -axes. Each cell type is randomly determined to either grow or non-grow according to the number density of growing cells in the system  $\rho_{\text{growth}}$ . The equilibrium volumes of cells are defined as

$$v_{i \text{ eq}}(t) = \begin{cases} (1 + V_{\text{growth}} t) v_0 & : \text{growing cell,} \\ v_0 & : \text{non-growing cell,} \end{cases} \quad (41)$$

where the equilibrium volumes of growing cells increase linearly with time at rate  $V_{\text{growth}}$ , as shown in Fig. 8. The model parameters representing cellular behaviors were set to values similar to those used in previous studies that used Honda's model (2004, 2008a, 2008b). All model parameters are shown in Table 1.

Figure 8c shows the applicable area of parameters where simulations could be performed. RNR simulations could be performed over the entire employed parameter space, whereas simulations without condition 4 could be performed only for parameters left of the solid blue line in Fig. 8c. In addition, simulations without condition 4 tend to fail as

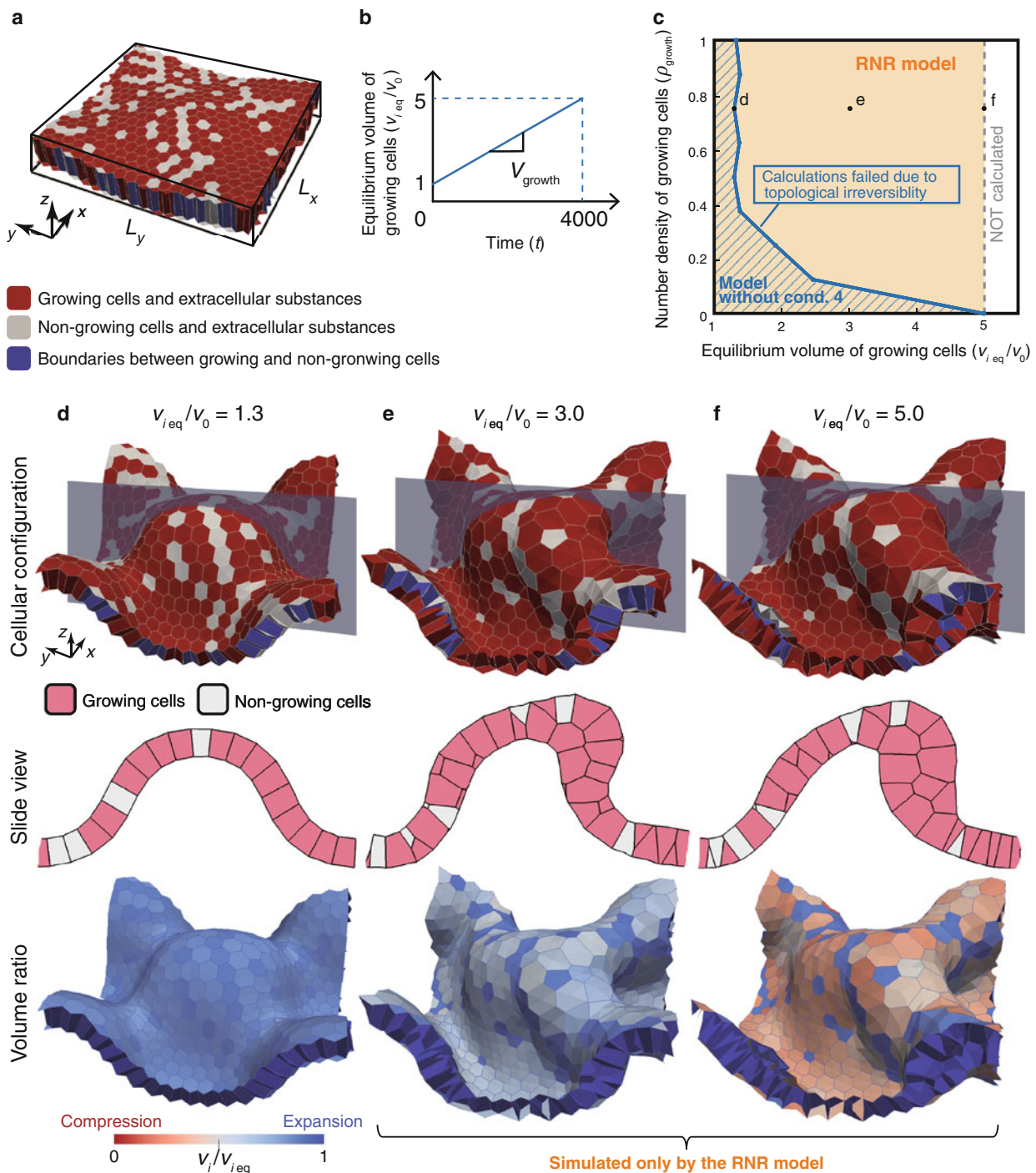


**Fig. 8** Simulations of tissue growth. **a** Initial condition of the simulations. Four hundred cells are aligned on a curved surface at regular intervals. Periodic boundaries are employed for the  $x$ - and  $y$ -axes. Red and gray cells indicate growing and non-growing cells, respectively. **b** Changes in the equilibrium volume of growing cells  $v_{i\text{eq}}$  as a function of time. **c** The applicable area of simulations using the RNR model (which includes condition 4) and a model without condition 4. The vertical and transverse axes indicate the number density of growing cells  $\rho_{\text{growth}}$  and the equilibrium volume of growing cells  $v_{i\text{eq}}/v_0$ , respectively. The shaded and orange areas indicate areas in which the RNR model and a model without condition 4 can be applied,

respectively. The area outside the dotted gray line ( $v_{i\text{eq}}/v_0 = 5.0$ ) indicates where calculations were not performed. Points  $d$ ,  $e$ , and  $f$  indicate the states with  $v_{i\text{eq}}/v_0 = 1.3$ ,  $3.0$ , and  $5.0$  at  $\rho_{\text{growth}} = 0.75$ , respectively. **d**, **e**, and **f** Snapshots of cellular configurations, slice views, and cellular volume ratios in states  $d$ ,  $e$ , and  $f$  in (c), respectively. Images of cross sections colored gray in the top figures are shown in the middle figures, where pink and white cells indicate growing and non-growing cells, respectively. The bottom figures show the cellular volume ratios  $v_i/v_{i\text{eq}}$ , color-coded according to the bottom-left legend. The cellular volume ratios are displayed only on tissue surfaces but not on cell-cell boundaries, denoted by dark blue

**Table 1** Model parameters

Symbol	Value	Description
$\eta$	1.0	Friction coefficient of vertex
$k^{cv}$	14	Constant of cellular volume elasticity
$\epsilon^{cc}$	1.0	Interface energy at cell–cell boundary
$\epsilon^{co}$	0.7	Interface energy at cell–outer space boundary
$v_0$	1.0	Characteristic volume of cell
$A^{ic}$	0.5	Amplitude of curved tissue under initial condition
$L_x$	13.2	Length of system box in $x$ axis
$L_y$	15.2	Length of system box in $y$ axis
$V_{\text{growth}}$	$1.0 \times 10^{-4}$	Growth rate of cellular volume
$\rho_{\text{growth}}$	0.0 – 1.0	Number density of growing cells in system
$\Delta t$	$1.0 \times 10^{-4}$	Integration time step
$\Delta t_r$	$1.0 \times 10^{-3}$	Time interval of network reconnection
$\Delta l_{\text{th}}$	$1.0 \times 10^{-3}$	Threshold length of network reconnection

either  $\rho_{\text{growth}}$  or  $v_i \text{ eq}$  increases. The points d, e, and f in Fig. 8c indicate the states with  $v_i \text{ eq}/v_0 = 1.3, 3.0$ , and  $5.0$  at  $\rho_{\text{growth}} = 0.75$ , respectively. Figure 8d–f show snapshots of cellular configurations, slice views, and cellular volume ratios that resulted from simulations for states d, e, and f, respectively. The cellular volume ratios  $v_i/v_i \text{ eq}$  reflect the magnitudes of forces exerted on cells by surrounding cells. In state d, both simulations showed the same tissue shape that was largely deformed with homogeneous curvatures, monolayered structures, and homogeneous distributions of cellular volume ratios (see Fig. 8d). In states e and f, only the RNR simulations could give results, and the tissue shapes had inhomogeneous curvatures, and the tissue structures changed from monolayer to multilayer. Furthermore, the cellular volume ratios in states e and f inhomogeneously decreased compared with those originally observed in state e (see also Mov. 1 in the Supplemental data).

## 4 Discussion

### 4.1 Geometrical reversibility of network reconnections

In reconnections with either condition H or the simple definition of polygonal centers, because geometrical gaps cannot be regulated by choosing the value of  $\Delta l_{\text{th}}$  [as shown in Eq. 8], the gaps occasionally become much larger than  $\Delta l_{\text{th}}$ . In contrast, in reconnections with conditions 1 and 2 employed in the RNR model, because these gaps approach zero in the first order of  $\Delta l_{\text{th}}$  as  $\Delta l_{\text{th}}$  decreases [as shown in Eqs. 7 and 15], patterns [H] and [I] become geometrically equivalent in the zero limit of  $\Delta l_{\text{th}}$  [as Eqs. 5 and 6]. Thus, reconnections with conditions 1 and 2 ensure geometrical reversibility, but those with either

condition H the simple definition of polygonal centers do not.

Because of geometrical reversibility, gaps of cellular geometrical properties are also suppressed. For example, in reconnections with the simple definition of polygonal centers, the area gaps of trigonal component of polygonal faces occasionally become much larger than the order of  $\Delta l_{\text{th}}$  under either condition 2 or H. These gaps become larger when a polygonal face deviates more from a flat plane as in Eq. (21). These large deviations are observed in simulations with several conditions depending on the cellular mechanical behaviors, as shown in Appendix.5. In contrast, in reconnections with conditions 1 and 2 employed in the RNR model, the area gaps of trigonal components are zero in the zero limit of  $\Delta l_{\text{th}}$  [as Eq. 20]. Therefore, area gaps of polygonal faces are also zero in the zero limit of  $\Delta l_{\text{th}}$ . Thus, condition 2 is useful for suppressing area gaps of polygonal faces, in particular, in cases of polygonal faces deviating significantly from a flat plane.

Because geometrically irreversible reconnections cause differences in the transition probabilities between bidirectional reconnections, geometrical irreversibility induces unintentional drifts in vertex dynamics. Such unintentional drifts can be suppressed in the RNR model.

### 4.2 Energetic consistency of network reconnections

In reconnections in cases employing either condition H or the simple definition of polygonal faces, because the sum of bidirectional energetic gaps cannot be regulated by choosing the value of  $\Delta l_{\text{th}}$  [as shown by Eq. 36], the gaps occasionally become much larger than the first order of  $\Delta l_{\text{th}}$ . In contrast, in reconnections with conditions 1 and 2 employed in the RNR model, because the sum of bidirectional energetic gaps



approaches zero in the first order of  $\Delta l_{th}$  as  $\Delta l_{th}$  decreases [as shown in Eq. 32], each energetic gap of a reconnection transition becomes equivalent to that of the reverse transition with the opposite sign in the zero limit of  $\Delta l_{th}$  [as shown in Eq. 27]. Thus, reconnections with conditions 1 and 2 ensure energetic consistency but those with condition H do not.

In addition, if the potential energies do not satisfy condition 3 (even if conditions 1 and 2 are satisfied), the sum of bidirectional energetic gaps becomes much larger than the order of  $\Delta l_{th}$ . Thus, condition 3 is necessary to ensure the energetic consistency.

If reconnections do not satisfy energetic consistency, they can generate or dissipate energy to induce unintentional drifts in vertex dynamics. Furthermore, from the viewpoint of computational simulations, because energetic inconsistency causes energetic jumps within a time step, numerical calculations tend to fail. Unintentional drifts induced by energetic inconsistency can be suppressed in the RNR model.

#### 4.3 Topological reversibility of network reconnections

Condition 4 employed in the RNR model avoids generating patterns  $[\alpha]$  and  $[\beta]$ , as shown in Sect. 3.3. In addition, as shown in Sect. 3.4, reconnection simulations without vertex dynamics demonstrate that simulations with condition 4 did not fail (at least for our employed parameter values), whereas simulations without condition 4 failed after two steps on an average because of topologically irreversible patterns. Thus, condition 4 resolves topological irreversibility in reconnections, and the RNR model satisfies topological reversibility.

Network patterns prohibited by condition 4(i) can correspond to the situation when four neighboring cells make contact just at a line. Also, network patterns prohibited by condition 4(ii) can correspond to the situation when cells are closely broken away by pushing forces exerted on them by surrounding cells. In the RNR model, condition 4 is introduced by assuming that these patterns can be relaxed within a time scale that is much less than that of tissue morphogenesis.

#### 4.4 Applicability for simulating tissue morphogenesis

Figure 8c shows that the model without condition 4 failed in simulating inhomogeneous large deformations beyond state d because of topological irreversibility. Because the tissue was largely deformed in state d, beyond which simulations using the model without condition 4 failed, we expected that irreversible network patterns tend to be generated during large deformation processes. In contrast, the RNR model (involving condition 4) was applicable for simulating inhomogeneous large deformations beyond state d. Thus, condition 4 employed in the RNR model extended its applicability

for simulating large deformations induced by increases in cell volume in 3D space. Beyond state d, inhomogeneous large deformations occur, cellular shapes are inhomogeneously deformed, and configurations are rearranged from monolayer to multilayer, as shown in states e and f.

#### 4.5 Limitations and future perspectives

Because condition 4 resolves the topological irreversibility, the RNR model can be applied to simulate large deformations induced by increases in cell volume. Resolving the topological irreversibility in condition 4 depends on network topological structures but not on the type of morphogenesis simulated. Therefore, the RNR model can be generally applied to simulate various types of morphogenesis involving inhomogeneous large deformations. For example, the RNR model can be used to simulate optic-cup formations (Eiraku et al. 2011), in which the tissue size drastically increases by proliferations, the tissue shape changes from convex to concave, and part of the tissue structure changes from monolayer to multilayer. Because such complicated deformations are induced by spatiotemporally regulated mechanics, it is necessary to analyze force fields such as those reflected by the volume ratios shown in Figs. 8d–f. Thus, the RNR model enables simulations of complex tissue morphogenesis in 3D space; until now, such simulations have not been attempted.

Tissue morphogenesis in development is often accompanied by cell proliferations that involve increases in both cell volumes and cell divisions (Davies 2005; Bellaiche and Segalen 2009). Because cell divisions are directed by microtubule alignments, they can generate anisotropic forces and transfers that induce inhomogeneous large deformations. Although cell divisions are important for tissue morphogenesis, 3D vertex models have not been applied to systems that involve them. This may be because topological irreversibility is caused by inhomogeneous large deformations of tissues. Therefore, the RNR model, which satisfies topological reversibility, can be applied to simulate the compressive large deformations that accompany tissue proliferations. Although cell divisions have not been modeled yet with the RNR model, dividing polyhedrons in the network is a possible way to express cell divisions. Condition 4 also be helpful for dividing polyhedrons in a way that avoids generating topologically irreversible patterns.

To investigate the effects of active cellular motions (such as cell migrations and intercalations) during tissue morphogenesis, we must distinguish cell motions from cellular drifts artificially induced by geometrical irreversibility and energetic inconsistency. The RNR model can suppress artificial drifts by employing conditions 1, 2, and 3. Thus, the RNR model is applicable to rearrangements driven by active cellular motions.

The RNR model can be applied to simulate the morphological dynamics of tissue composed of thousands of cells on the basis of the mechanical interactions among cells. In addition, anisotropic and inhomogeneous behaviors on the scale of intracellular structures, such as apical constrictions and cell–cell adhesions, can be expressed on the scale of cell–cell boundaries by designing functions of the potential energy. However, tissue morphogenesis is also affected by the dynamics of more detailed structures, such as actin fibers, microtubules, and morphogen molecules. To investigate the effects of these structures, we consider combining the RNR model with more detailed models (Jamali et al. 2010; Inoue and Adachi 2011).

Morphogenesis is also likely affected by fluctuations, such as force oscillations of apical constrictions driven by actomyosins on actin fibers (Solon et al. 2009; Martin et al. 2009; Blanchard et al. 2010). When simulating the dynamics of systems involving fluctuations, it will become further important to suppress unintentional drifts in vertex dynamics generated by reconnections (see Sects. 4.1, 4.2). This is because networks are more frequently reconnected by fluctuations, and unintentional drifts can accumulate to enhance the abnormal cell rearrangements. If fluctuation strength is much greater than the energy gaps in reconnections, unintentional drifts will be small enough that they can be ignored. In contrast, if fluctuation strength is of an order similar to or less than the energy gaps in reconnections, then unintentional drifts cannot be ignored. Thus, conditions 1, 2, and 3 introduced in the RNR model will be occasionally helpful when using 3D vertex models to simulate the dynamics of systems involving fluctuations.

Chemical factors, such as morphogen molecules, also play an important role in tissue morphogenesis, and these factors can interact with cellular mechanical behaviors (Heisenberg et al. 2000; Letizia et al. 2011; Eiraku et al. 2011; Bellaiche and Segalen 2009). Interactions between chemical and mechanical factors may play a key role in self-organizing tissues in development. Cellular mechanical behaviors can be expressed by functions of the potential energy, while chemical behaviors are yet to be modeled. Modeling these mechano-chemical couplings is a challenging opportunity to expand the RNR model in the future.

These expansions will enhance the reality and increase the reliability of RNR simulations of tissue morphogenesis. Thus, such an expanded RNR model will enable qualitative and quantitative predictions *in silico*; we will learn how tissue formation proceeds under arbitrary realistic and unrealistic conditions. Such *in silico* recapitulations may reveal mechanisms that have not been recognized by experimental studies; for example, tissue morphogenesis may be surprisingly robust against perturbations. The RNR model will contribute to innovation in computational developmental biomechanics.

## 5 Conclusion

To simulate large deformations of multicellular aggregates during tissue morphogenesis in 3D space, we developed the RNR model based on the concept of 3D vertex formulations. The following were introduced in the RNR model: (1) a new definition of the shapes of polygonal faces between cellular polyhedrons, (2) an improved condition for network reconnections, and (3) a new condition for potential energy functions. We theoretically confirmed that energetic consistency in reconnections is satisfied when conditions 1, 2, and 3 are satisfied. In addition, the following was introduced in the RNR model: (4) a new constraint condition on network topology. Simulations of network reconnections confirmed that condition 4 resolves their topological irreversibility. To demonstrate the applicability of the RNR model, we simulated tissue deformations of a growing cell sheet under compression. We found that the RNR model is applicable for simulating large deformations with increasing cell volumes, whereas the model without condition 4 is not. During these tissue deformations, the curvatures of tissue shapes became inhomogeneous, and tissue structures changed from monolayer to multilayer. Therefore, our proposed RNR model can successfully simulate inhomogeneous large deformations.

**Acknowledgments** The authors appreciate valuable comments from Prof. H. Honda at the University of Hyogo, Japan. This study was partly supported by the Funding Program for Next Generation World-Leading Researchers (LR017) from the Ministry of Education, Culture, Sports, Science and Technology in Japan. Satoru Okuda was supported by the Japan Society for the Promotion of Science (JSPS) as a JSPS fellow. Yasuhiro Inoue was supported by Grant-in-Aid for Scientific Research on Innovative Areas from the Ministry of Education, Culture, Sports, Science and Technology of Japan.

## Appendix

### 1. Definitions of vertex positions after reconnections

In this section, we discuss the network reconnections shown in Fig. 3.

#### 1.1 Vertex positions after the reconnection from [H] to [I] in the RNR model

The position vectors of vertices 10 and 11, denoted by  $\mathbf{r}_{10}$  and  $\mathbf{r}_{11}$ , respectively, are defined as follows:

$$\mathbf{r}_{10} = \mathbf{r}_0^H + 0.5\Delta l_{th}\mathbf{u}_T^H, \quad (42)$$

$$\mathbf{r}_{11} = \mathbf{r}_0^H - 0.5\Delta l_{th}\mathbf{u}_T^H, \quad (43)$$

where  $\mathbf{r}_{10}$  and  $\mathbf{r}_{11}$  are placed on the line along  $\mathbf{u}_T^H$  passing through  $\mathbf{r}_0^H$ . Vector  $\mathbf{u}_T^H$  indicates a unit vector normal to the trigonal face 7–8–9 as



$$\mathbf{u}_T^H = \frac{(\mathbf{r}_8 - \mathbf{r}_7) \times (\mathbf{r}_9 - \mathbf{r}_7)}{|\mathbf{r}_8 - \mathbf{r}_7| |\mathbf{r}_9 - \mathbf{r}_7|}. \quad (44)$$

Vector  $\mathbf{r}_0^H$  in Eqs. (42) and (43) indicates the position vector of the center of mass of the trigonal face 7–8–9 as

$$\mathbf{r}_0^H = \frac{\mathbf{r}_7 + \mathbf{r}_8 + \mathbf{r}_9}{3}. \quad (45)$$

*Vertex positions after the reconnection from [I] to [H] in the RNR model*

The position vectors of vertices 7, 8, and 9, denoted by  $\mathbf{r}_7$ ,  $\mathbf{r}_8$ , and  $\mathbf{r}_9$ , respectively, are defined as follows:

$$\mathbf{r}_7 = \mathbf{r}_0^I + \frac{\Delta l_{th}}{l_{max}} \mathbf{v}_{0-7}, \quad (46)$$

$$\mathbf{r}_8 = \mathbf{r}_0^I + \frac{\Delta l_{th}}{l_{max}} \mathbf{v}_{0-8}, \quad (47)$$

$$\mathbf{r}_9 = \mathbf{r}_0^I + \frac{\Delta l_{th}}{l_{max}} \mathbf{v}_{0-9}, \quad (48)$$

where  $\mathbf{r}_7$ ,  $\mathbf{r}_8$ , and  $\mathbf{r}_9$  are placed in a plane face normal to  $\mathbf{u}_T^I$  passing through  $\mathbf{r}_0^I$ . Vector  $\mathbf{u}_T^I$  indicates a unit vector from vertex 10 to vertex 11 as

$$\mathbf{u}_T^I = \frac{\mathbf{r}_{10} - \mathbf{r}_{11}}{|\mathbf{r}_{10} - \mathbf{r}_{11}|}. \quad (49)$$

Vector  $\mathbf{r}_0^I$  in Eqs. (46–48) indicates the position vector of the midpoint of the line 10–11 as

$$\mathbf{r}_0^I = \frac{\mathbf{r}_{10} + \mathbf{r}_{11}}{2}. \quad (50)$$

Vectors  $\mathbf{v}_{0-7}$ ,  $\mathbf{v}_{0-8}$ , and  $\mathbf{v}_{0-9}$  in Eqs. (46–48) are defined as follows:

$$\mathbf{v}_{0-7} = \mathbf{w}_{0-7} - (\mathbf{w}_{0-7} \cdot \mathbf{u}_T^I) \mathbf{u}_T^I, \quad (51)$$

$$\mathbf{v}_{0-8} = \mathbf{w}_{0-8} - (\mathbf{w}_{0-8} \cdot \mathbf{u}_T^I) \mathbf{u}_T^I, \quad (52)$$

$$\mathbf{v}_{0-9} = \mathbf{w}_{0-9} - (\mathbf{w}_{0-9} \cdot \mathbf{u}_T^I) \mathbf{u}_T^I, \quad (53)$$

where  $\mathbf{v}_{0-7}$ ,  $\mathbf{v}_{0-8}$ , and  $\mathbf{v}_{0-9}$  are vectors of  $\mathbf{w}_{0-7}$ ,  $\mathbf{w}_{0-8}$ , and  $\mathbf{w}_{0-9}$ , respectively, projected onto a plane face normal to  $\mathbf{u}_T^I$ . The vectors  $\mathbf{w}_{0-7}$ ,  $\mathbf{w}_{0-8}$ , and  $\mathbf{w}_{0-9}$  are defined as

$$\mathbf{w}_{0-7} = \frac{1}{2} \left( \frac{\mathbf{r}_1 - \mathbf{r}_0^I}{|\mathbf{r}_1 - \mathbf{r}_0^I|} + \frac{\mathbf{r}_4 - \mathbf{r}_0^I}{|\mathbf{r}_4 - \mathbf{r}_0^I|} \right), \quad (54)$$

$$\mathbf{w}_{0-8} = \frac{1}{2} \left( \frac{\mathbf{r}_2 - \mathbf{r}_0^I}{|\mathbf{r}_2 - \mathbf{r}_0^I|} + \frac{\mathbf{r}_5 - \mathbf{r}_0^I}{|\mathbf{r}_5 - \mathbf{r}_0^I|} \right), \quad (55)$$

$$\mathbf{w}_{0-9} = \frac{1}{2} \left( \frac{\mathbf{r}_3 - \mathbf{r}_0^I}{|\mathbf{r}_3 - \mathbf{r}_0^I|} + \frac{\mathbf{r}_6 - \mathbf{r}_0^I}{|\mathbf{r}_6 - \mathbf{r}_0^I|} \right). \quad (56)$$

Variable  $l_{max}$  in Eqs. (46–48) indicates the maximum length of  $|\mathbf{v}_{0-8} - \mathbf{v}_{0-7}|$ ,  $|\mathbf{v}_{0-9} - \mathbf{v}_{0-8}|$ , and  $|\mathbf{v}_{0-7} - \mathbf{v}_{0-9}|$ , which indicate edges of a triangle composed of  $\mathbf{v}_{0-7}$ ,  $\mathbf{v}_{0-8}$ , and  $\mathbf{v}_{0-9}$ .

## 2. Geometrical gaps in the vertex positions generated by network reconnections

To estimate the geometrical gaps in the vertex positions before and after the network reconnections shown in Fig. 3, changes in the distance from point 0 to vertices 7, 8, 9, 10, and 11 between patterns [H] and [I] are measured before and after the reconnections using conditions H and 2.

### 2.1 Processes between patterns [H] and [I] under condition 2

In the RNR model, the network is reconnected according to the rule shown in Fig. 3 under condition 2. The maximum length from point 0 to vertices 7, 8, and 9, denoted by  $\Delta r_{H \leftrightarrow O}^{vt}$ , satisfies the following relationship:

$$\Delta r_{H \leftrightarrow O}^{vt} \leq \Delta l_{th}. \quad (57)$$

Because point 0 in pattern [I] is located at the midpoint of an edge composed of vertices 10 and 11 in reconnection processes between patterns [O] and [I], the maximum length from point 0 to vertices 10 and 11, denoted by  $\Delta r_{O \leftrightarrow I}^{vt}$ , satisfies the following relationship:

$$\Delta r_{O \leftrightarrow I}^{vt} \leq \frac{1}{2} \Delta l_{th}. \quad (58)$$

Thus, the maximum length from point 0 to the five vertices 7, 8, 9, 10, and 11, denoted by  $\Delta r_{O \leftrightarrow I}^{vt}$ , satisfies multilayer relationship:

$$\Delta r_{H \leftrightarrow I}^{vt} \leq \Delta l_{th}, \quad (59)$$

which means that the gaps in the vertex positions generated by reconnections are equal to or less than  $\Delta l_{th}$  if condition 2 is employed (see Fig. 4).

### 2.2 Processes between patterns [H] and [I] under condition H

According to the rule shown in Fig. 3 under condition H, because the edge related to reconnections from [I] to [H] is only an edge between vertices 10 and 11, gaps in the vertex positions in reconnections from [I] to [H] are in the first order of  $\Delta l_{th}$ , as in the RNR model. However, three edges are related to reconnections from [H] to [I]. Hence, gaps in reconnection processes from [H] to [I] can be different from those in the RNR model.

According to the rule shown in Fig. 3 under condition 2, the maximum length from point 0 to vertices 7, 8, and 9, denoted by  $\Delta r_{H \rightarrow O}^{vt}$ , satisfies the following relationship:

$$\Delta r_{H \rightarrow O}^{\text{vt}} \leq \Delta l_{\max}, \quad (60)$$

where  $\Delta l_{\max}$  indicates the maximum length from point 0 to vertices 7, 8, and 9. The maximum length from point 0 to vertices 7, 8, 9, 10, and 11, denoted by  $\Delta r_{H \rightarrow I}^{\text{vt}}$ , satisfies the following relationship:

$$\Delta r_{H \rightarrow I}^{\text{vt}} \leq \Delta l_{\max}. \quad (61)$$

Thus, we have

$$\Delta r_{H \leftrightarrow I}^{\text{vt}} \leq \Delta l_{\max}, \quad (62)$$

which means that the gaps in the vertex positions due to reconnections are equal to or larger than the first order of  $\Delta l_{\text{th}}$ , when  $\Delta l_{\max}$  is larger than  $\Delta l_{\text{th}}$ .

### 3. Displacements of the center positions of polygonal faces

To analyze the center displacements generated by reconnections,  $a_i^{\text{std}}$  and  $b_i^{\text{std}}$  are defined as the numerator and denominator of Eq. (3), respectively:

$$a_i^{\text{std}} = \sum_{j(i)}^{\text{vertex}} |r_{j+1(i)} - r_{j(i)}| \frac{r_{j+1(i)} + r_{j(i)}}{2}, \quad (63)$$

$$b_i^{\text{std}} = \sum_{j(i)}^{\text{vertex}} |r_{j+1(i)} - r_{j(i)}|. \quad (64)$$

#### 3.1 Effects of vertex movements

When the  $s$ th vertex in the  $i$ th polygonal face is displaced by  $\Delta r_{s(i)}$  (see Fig. 5a), the center displacement of the  $i$ th polygonal face  $\Delta^{\text{d}} r_i^{\text{pf}}$  is

$$\Delta^{\text{d}} r_i^{\text{pf}} = \frac{a_{s(i)}^{\text{d}}}{b_{s(i)}^{\text{d}}} - \frac{a_i^{\text{std}}}{b_i^{\text{std}}}, \quad (65)$$

where

$$\begin{aligned} a_{s(i)}^{\text{d}} = & a_i^{\text{std}} - |r_{s(i)} - r_{s-1(i)}| \frac{r_{s(i)} + r_{s-1(i)}}{2} \\ & - |r_{s+1(i)} - r_{s(i)}| \frac{r_{s+1(i)} + r_{s(i)}}{2} \\ & + |(r_{j(i)} + \Delta r_{s(i)}) - r_{j-1(i)}| \frac{(r_{j(i)} + \Delta r_{s(i)}) + r_{j-1(i)}}{2} \\ & + |r_{s+1(i)} - (r_{s(i)} + \Delta r_{s(i)})| \frac{r_{s+1(i)} + (r_{s(i)} + \Delta r_{s(i)})}{2}, \end{aligned} \quad (66)$$

and

$$\begin{aligned} b_{s(i)}^{\text{d}} = & b_i^{\text{std}} - |r_{s(i)} - r_{s-1(i)}| - |r_{s+1(i)} - r_{s(i)}| \\ & + |(r_{s(i)} + \Delta r_{s(i)}) - r_{s-1(i)}| \\ & + |r_{s+1(i)} - (r_{s(i)} + \Delta r_{s(i)})|. \end{aligned} \quad (67)$$

Then,  $\Delta^{\text{d}} r_i^{\text{pf}}$  is rewritten as

$$\begin{aligned} \Delta^{\text{d}} r_i^{\text{pf}} = & \frac{1}{b^{\text{d}} b^{\text{std}}} \left\{ \left( |(r_{s(i)} + \Delta r_{s(i)}) - r_{s-1(i)}| \right. \right. \\ & \left. \left. - |r_{s(i)} - r_{s-1(i)}| \right) \left( b^{\text{std}} \frac{r_{s(i)} + r_{s-1(i)}}{2} - a^{\text{std}} \right) \right. \\ & \left. + \left( |r_{s+1(i)} - (r_{s(i)} + \Delta r_{s(i)})| \right. \right. \\ & \left. \left. - |r_{s+1(i)} - r_{s(i)}| \right) \left( b^{\text{std}} \frac{r_{s+1(i)} + r_{s(i)}}{2} - a^{\text{std}} \right) \right\}. \end{aligned} \quad (68)$$

We find

$$|\Delta^{\text{d}} r_i^{\text{pf}}| = O(|\Delta r_{s(i)}|), \quad (69)$$

which implies that center displacements are in the first order of the vertex displacement, supposing that the vertex displacement is much smaller than the length scale of the polygonal face.

#### 3.2 Effects of vertex additions

When a single vertex is newly generated between the  $t$ th and  $(t+1)$ th vertices in the  $i$ th polygonal face (see Fig. 5b), the center displacement of the  $i$ th polygonal face  $\Delta^{\text{p}} r_i^{\text{pf}}$  is

$$\Delta^{\text{p}} r_i^{\text{pf}} = \frac{a^{\text{p}}}{b^{\text{p}}} - \frac{a^{\text{std}}}{b^{\text{std}}}, \quad (70)$$

where

$$\begin{aligned} a^{\text{p}} = & a^{\text{std}} - |r_{j+1(i)} - r_{t(i)}| \frac{r_{t+1(i)} + r_{t(i)}}{2} \\ & + |r_{\text{plus}} - r_{t(i)}| \frac{r_{\text{plus}} + r_{t(i)}}{2} \\ & + |r_{t+1(i)} - r_{\text{plus}}| \frac{r_{t+1(i)} + r_{\text{plus}}}{2}, \end{aligned} \quad (71)$$

and

$$\begin{aligned} b^{\text{p}} = & b^{\text{std}} - |r_{t+1(i)} - r_{t(i)}| \\ & + |r_{\text{plus}} - r_{t(i)}| + |r_{t+1(i)} - r_{\text{plus}}|. \end{aligned} \quad (72)$$

Then,  $\Delta^{\text{p}} r_i^{\text{pf}}$  is rewritten as

$$\begin{aligned} \Delta^{\text{p}} r_i^{\text{pf}} = & \frac{1}{b^{\text{p}} b^{\text{std}}} \left\{ |r_{\text{plus}} - r_{t(i)}| \left( \frac{r_{\text{plus}} + r_{t(i)}}{2} b^{\text{std}} - a^{\text{std}} \right) \right. \\ & + |r_{t+1(i)} - r_{\text{plus}}| \left( \frac{r_{t+1(i)} + r_{\text{plus}}}{2} b^{\text{std}} - a^{\text{std}} \right) \\ & \left. - |r_{t+1(i)} - r_{t(i)}| \left( \frac{r_{t+1(i)} + r_{t(i)}}{2} b^{\text{std}} - a^{\text{std}} \right) \right\}, \end{aligned} \quad (73)$$

where we define

$$\mathbf{r}_{\text{plus}} = \mathbf{r}_{t(i)} + \Delta \mathbf{r}_{\text{plus}}. \quad (74)$$

Assuming Eq. (10), we find

$$|\Delta^{\text{p}} \mathbf{r}_i^{\text{pf}}| = O(|\Delta \mathbf{r}_{\text{plus}}|), \quad (75)$$

which implies that center displacements are in the first order of the distance between the new vertex and a single neighboring vertex, supposing that the distance is much smaller than the length scale of the polygonal face.

### 3.3 Effects of vertex eliminations

When the  $u$ th vertex in the  $i$ th polygonal face is eliminated (see Fig. 5c), the center displacement of the  $i$ th polygonal face  $\Delta^{\text{m}} \mathbf{r}_i^{\text{pf}}$  is

$$\Delta^{\text{m}} \mathbf{r}_i^{\text{pf}} = \frac{\mathbf{a}^{\text{m}}}{b^{\text{m}}} - \frac{\mathbf{a}^{\text{std}}}{b^{\text{std}}}, \quad (76)$$

where

$$\begin{aligned} \mathbf{a}^{\text{m}} = \mathbf{a}^{\text{std}} & - |\mathbf{r}_{u(i)} - \mathbf{r}_{u-1(i)}| \frac{\mathbf{r}_{u(i)} + \mathbf{r}_{u-1(i)}}{2} \\ & - |\mathbf{r}_{u+1(i)} - \mathbf{r}_{u(i)}| \frac{\mathbf{r}_{u+1(i)} + \mathbf{r}_{u(i)}}{2} \\ & + |\mathbf{r}_{u+1(i)} - \mathbf{r}_{u-1(i)}| \frac{\mathbf{r}_{u+1(i)} + \mathbf{r}_{u-1(i)}}{2}, \end{aligned} \quad (77)$$

and

$$\begin{aligned} b^{\text{m}} = b^{\text{std}} & - |\mathbf{r}_{u(i)} - \mathbf{r}_{u-1(i)}| - |\mathbf{r}_{u+1(i)} - \mathbf{r}_{u(i)}| \\ & + |\mathbf{r}_{u+1(i)} - \mathbf{r}_{u-1(i)}|. \end{aligned} \quad (78)$$

Then,  $\Delta^{\text{m}} \mathbf{r}_i^{\text{pf}}$  is rewritten as

$$\begin{aligned} \Delta^{\text{m}} \mathbf{r}_i^{\text{pf}} = \frac{1}{b^{\text{m}} b^{\text{std}}} & \left\{ -|\mathbf{r}_{u(i)} - \mathbf{r}_{u-1(i)}| \right. \\ & \times \left( \frac{\mathbf{r}_{u(i)} + \mathbf{r}_{u-1(i)}}{2} b^{\text{std}} - \mathbf{a}^{\text{std}} \right) \\ & - |\mathbf{r}_{u+1(i)} - \mathbf{r}_{u(i)}| \left( \frac{\mathbf{r}_{u+1(i)} + \mathbf{r}_{u(i)}}{2} b^{\text{std}} - \mathbf{a}^{\text{std}} \right) \\ & + |\mathbf{r}_{u+1(i)} - \mathbf{r}_{u-1(i)}| \\ & \times \left. \left( \frac{\mathbf{r}_{u+1(i)} + \mathbf{r}_{u-1(i)}}{2} b^{\text{std}} - \mathbf{a}^{\text{std}} \right) \right\}, \end{aligned} \quad (79)$$

where we define

$$\mathbf{r}_{u(i)} = \mathbf{r}_{u-1(i)} + \Delta \mathbf{r}_{\text{minus}}. \quad (80)$$

Assuming Eq. (12), we find

$$|\Delta^{\text{m}} \mathbf{r}_i^{\text{pf}}| = O(|\Delta \mathbf{r}_{\text{minus}}|), \quad (81)$$

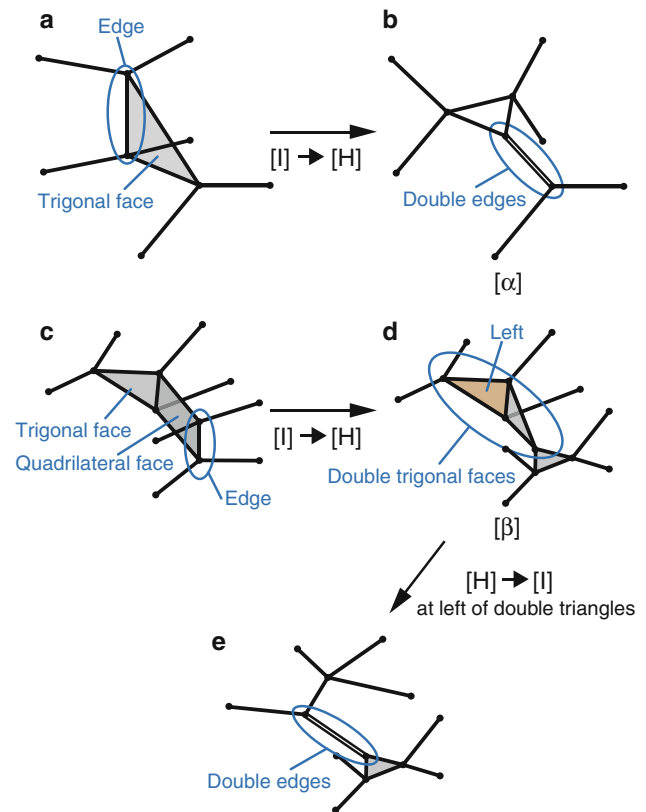


**Fig. 9** Examples of generation processes of topological patterns to which the reconnection rule in Fig. 3 cannot be applied. **a** An example of a pattern possibly reconnected to  $[\alpha]$ . Note that there is a trigonal face. The reconnection from [I] to [H] is applied to one of the edges composing the trigonal face. **b** Pattern  $[\alpha]$  reconnected from the pattern in (a). Note that there are double edges that connect to the same two vertices. **c** An example of a pattern possibly reconnected to  $[\beta]$ . Note that a trigonal face and a quadrilateral face reside next to each other. The reconnection from [I] to [H] is applied to an edge of the quadrilateral face located opposite the trigonal face. **d** Pattern  $[\beta]$  reconnected from the pattern in (c). Note that there are two neighboring trigonal faces. **e** An example of a pattern possibly reconnected from  $[\beta]$ , which has double edges. The reconnection from [H] to [I] was applied to the left of the double trigonal faces in (d)

which implies that center displacements are in the first order of the distance between the eliminated vertex and a single neighboring vertex, supposing that the distance is much smaller than the length scale of the polygonal face.

### 4. Two irreversible patterns generated by reconnections

There are at least two topological patterns of a network to which the reconnection rule cannot be applied:  $[\alpha]$  and  $[\beta]$  in Fig. 9. Pattern  $[\alpha]$  is generated, for example, when a reconnection from [I] to [H] is applied to one of the edges composing the trigonal face in Fig. 9a. The network including  $[\alpha]$  cannot be reconnected, for example, when a reconnection from [I] to [H] is applied to one of the double edges in Fig. 9b. This is because the topology of the network after

reconnection cannot be determined. Note that this process from a to b in Fig. 9 does not occur in Honda's model. This is because edges involved in trigonal faces are excluded as candidates for pattern [I] in Honda's model.

Pattern  $[\beta]$  is generated, for example, when a reconnection from [H] to [I] is applied to a trigonal face neighboring two quadrilateral faces in Fig. 9c. For example, when a reconnection from [H] to [I] is applied to the left of the double trigonal faces in Fig. 9d, the network including  $[\beta]$  creates double edges in Fig. 9e. This is because the topology of the network after the reconnection includes pattern  $[\alpha]$ . There are some other patterns reconnected to  $[\alpha]$  or  $[\beta]$  in the reconnection rule shown in Fig. 3.

### 5. Simulations for area gap estimations under the simple definition of a polygonal center

Employing the simple definition of a polygonal center given in Eq. (16), area gaps of polygonal faces are generated in reconnections as in Eqs. (24, 25), and (26). By comparison, employing condition 1, these area gaps can be suppressed as in Eq. (23). In particular, when a polygonal face deviates significantly from a flat plane, condition 1 will be more valuable for suppressing larger area gaps as in Eq. (21). However, in simulations using 3D vertex models, it is not known to what extent polygonal faces deviate from a flat plane. Then, to evaluate the approximate effectiveness of condition 1, we estimate the approximate area gaps of polygonal faces under the simple definition using the RNR simulation.

In this simulation,  $\rho_{\text{growth}}$  is set to 0.75, and  $\epsilon^{\text{cc}}$  and  $\epsilon^{\text{co}}$  are set to  $\epsilon_0$  and  $0.7\epsilon_0$ , respectively, where  $\epsilon_0$  indicates an interface energy strength modulus. To vary the deviation of polygonal faces from a flat plane, the strengths of the parameters  $\epsilon^{\text{cc}}$  and  $\epsilon^{\text{co}}$  are varied. The other conditions used in this simulation are equivalent to those in Sect. 3.5.

The area gaps are estimated from vertex coordinates at the time when  $v_{i \text{ eq}}/v_0 = 5.0$ . Assuming that a single new vertex is added just at the position of an already existing vertex composing a polygonal face, the area gaps of the polygonal faces before and after the vertex addition are measured (see Fig. 10a, b). Based on this assumption, these processes correspond to vertex addition or elimination in reconnections with  $\Delta l_{\text{th}} = 0$ .

Figure 10c shows estimated area gaps as a function of  $\epsilon_0$ . The area gaps are normalized by areas of individual polygonal faces before vertex additions. Blue, red, and green lines indicate the mean, standard deviation, and the maximum values of the area gaps, respectively. These values are averaged for all vertices of polygonal faces during states within  $3 \leq v_{i \text{ eq}}/v_0 \leq 4$ . The standard deviation of the gaps became much larger than the mean. This is because tissue shapes inhomogeneously undulate by location. In addition, with decreasing values of  $\epsilon_0$ , area gaps increase. For example,

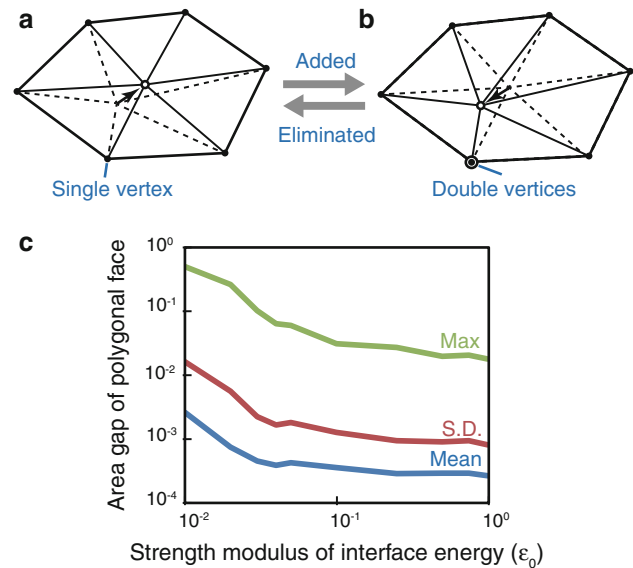


**Fig. 10** Estimation of area gaps under the simple definition of a polygonal center. **a** Position of a polygonal center when a single vertex already exists at the location of the  $j$ th vertex position. **b** Position of a polygonal center when double vertices exist at the location of the  $j$ th vertex position. **c** Area gaps under the simple definition as a function of an interface energy strength modulus  $\epsilon_0$ . The area gaps, which are estimated as those between **a** and **b**, are normalized by areas of individual polygonal faces before vertex additions. Blue, red, and green lines indicate the mean, SD, and the maximum values of the area gaps, respectively

while the maximum value of the area gaps was about 0.02 in the state with  $\epsilon_0 = 1.0$ , this value was about 0.5 in the state with  $\epsilon_0 = 0.01$ . Thus, depending on the cellular mechanical behaviors, area gaps of polygonal faces can occasionally be too large to ignore. In contrast, when employing condition 1, because the area gaps of polygonal faces depend on  $\Delta l_{\text{th}}$  as in Eq. (21), the estimated area gaps are zero independent of the cellular mechanical behaviors. Thus, condition 1 is useful for suppressing the area gaps of polygonal faces.

### References

- Bellaiche Y, Segalen M (2009) Cell division orientation and planar cell polarity pathways. *Semin Cell Dev Biol* 20(8):972–977
- Blanchard GB, Murugesu S et al (2010) Cytoskeletal dynamics and supracellular organisation of cell shape fluctuations during dorsal closure. *Development* 137(16):2743–2752
- Bragg L, Nye JF (1947) A dynamical model of a crystal structure. *Proc R Soc Lond A Math Phys Sci* 190(1023):474–481
- Davies JA (2005) Mechanisms of morphogenesis: the creation of biological form. Elsevier Academic Press, Burlington
- Eiraku M, Takata N et al (2011) Self-organizing optic-cup morphogenesis in three-dimensional culture. *Nature* 472(7341):51–56
- Eiraku M, Adachi T et al (2012) Relaxation-expansion model for self-driven retinal morphogenesis. *Bioessays* 34(1):17–25

- Farhadifar R, Röper JC et al (2007) The influence of cell mechanics, cell-cell interactions, and proliferation on epithelial packing. *Curr Biol* 17(24):2095–2104
- Forgacs G, Newman SA (2005) *Biological physics of the developing embryo*. Cambridge University Press, New York
- Friedlander DR, Mège RM et al (1989) Cell sorting-out is modulated by both the specificity and amount of different cell-adhesion molecules (CAMs) expressed on cell-surfaces. *Proc Natl Acad Sci USA* 86(18):7043–7047
- Fuchizaki K, Kusaba T et al (1995) Computer modelling of three-dimensional cellular pattern growth. *Philos Mag B* 71(3):333–357
- Heisenberg CP, Tada M et al (2000) Silberblick/Wnt11 mediates convergent extension movements during zebrafish gastrulation. *Nature* 405(6782):76–81
- Honda H, Ogita Y et al (1982) Cell movements in a living mammalian tissue: long-term observation of individual cells in wounded corneal endothelia of cats. *J Morphol* 174(1):25–39
- Honda H, Tanemura M et al (2004) A three-dimensional vertex dynamics cell model of space-filling polyhedra simulating cell behavior in a cell aggregate. *J Theor Biol* 226(4):439–453
- Honda H, Motosugi N et al (2008) Computer simulation of emerging asymmetry in the mouse blastocyst. *Development* 135(8):1407–1414
- Honda H, Nagai T et al (2008) Two different mechanisms of planar cell intercalation leading to tissue elongation. *Dev Dyn* 237(7):1826–1836
- Ingber DE, Mammoto T (2010) Mechanical control of tissue and organ development. *Development* 137(9):1407–1420
- Inoue Y, Adachi T (2011) Coarse-grained Brownian ratchet model of membrane protrusion on cellular scale. *Biomech Model Mechanobiol* 10(4):495–503
- Jamali Y, Azimi M, et al (2010) A sub-cellular viscoelastic model for cell population mechanics. *PLoS One* 5(8)
- Kikuchi R (1956) Shape distribution of two-dimensional soap froths. *J Chem Phys* 24(4):861–867
- Lecuit T, Lenne PF (2007) Cell surface mechanics and the control of cell shape, tissue patterns and morphogenesis. *Nat Rev Mol Cell Biol* 8(8):633–644
- Lecuit T, Rauzi M et al (2008) Nature and anisotropy of cortical forces orienting *Drosophila* tissue morphogenesis. *Nat Cell Biol* 10(12):1401–1410
- Lecuit T, Rauzi M et al (2010) Planar polarized actomyosin contractile flows control epithelial junction remodelling. *Nature* 468(7327):1110–1114
- Letizia A, Sotillos S et al (2011) Regulated Crb accumulation controls apical constriction and invagination in *Drosophila* tracheal cells. *J Cell Sci* 124(2):240–251
- Martin AC, Kaschube M et al (2009) Pulsed contractions of an actin-myosin network drive apical constriction. *Nature* 457(7228):495–499
- Nagai T, Honda H (2001) A dynamic cell model for the formation of epithelial tissues. *Philos Mag B* 81(7):699–719
- Nagai T, Honda H (2009) Computer simulation of wound closure in epithelial tissues: Cell-basal-lamina adhesion. *Phys Rev E Stat Nonlin Soft Matter Phys* 80(6):061903
- Nagai T, Kawasaki K et al (1988) Vertex dynamics of two-dimensional cellular-patterns. *J Phys Soc Jpn* 57(7):2221–2224
- Nagai T, Ohta S et al (1990) Computer simulation of cellular pattern growth in two and three dimensions. *Phase Transit* 28:177–211
- Odell GM, Oster G et al (1981) The mechanical basis of morphogenesis. 1. Epithelial folding and invagination. *Dev Biol* 85(2):446–462
- Rauzi M, Verant P et al (2008) Nature and anisotropy of cortical forces orienting *Drosophila* tissue morphogenesis. *Nat Cell Biol* 10(12):1401–1410
- Solon J, Kaya-Copur A et al (2009) Pulsed forces timed by a ratchet-like mechanism drive directed tissue movement during dorsal closure. *Cell* 137(7):1331–1342
- Staple DB, Farhadifar R et al (2010) Mechanics and remodelling of cell packings in epithelia. *Eur Phys J E Soft Matter* 33(2):117–127
- Taniguchi K, Maeda R et al (2011) Chirality in planar cell shape contributes to left-right asymmetric epithelial morphogenesis. *Science* 333(6040):339–341
- VanEssen DC (1997) A tension-based theory of morphogenesis and compact wiring in the central nervous system. *Nature* 385(6614):313–318
- Weaire D, Kermode JP (1983) Computer-simulation of a two-dimensional soap froth. 1. Method and motivation. *Philos Mag B* 48(3):245–259
- Weaire D, Kermode JP (1984) Computer-simulation of a two-dimensional soap froth. 2. Analysis of results. *Philos Mag B* 50(3):379–395
- Weliky M, Oster G (1990) The mechanical basis of cell rearrangement. 1. Epithelial morphogenesis during fundulus epiboly. *Development* 109(2):373–386